Carbon 107 (2016) 885–894

Contents lists available at ScienceDirect

Carbon

journal homepage: www.elsevier.com/locate/carbon

Dispersion-corrected DFT investigation on defect chemistry and potassium migration in potassium-graphite intercalation compounds for potassium ion batteries anode materials

Zhenming Xu [a], Xiaojun Lv [a, *], Jiangan Chen [b], Liangxing Jiang [a], Yanqing Lai [a], Jie Li [a]

[a] School of Metallurgy and Environment, Central South University, Changsha 410083, PR China
[b] Faculty of Resource and Environmental Engineering, Jiangxi University of Science and Technology, Ganzhou 341000, PR China

ARTICLE INFO

Article history:
Received 14 May 2016
Received in revised form
25 June 2016
Accepted 27 June 2016
Available online 28 June 2016

ABSTRACT

The first-principles calculations based on the density function theory (DFT) with the dispersion-corrected DFT-D2 method were performed to investigate the structure, energetics, electronic structure, defects properties and cation migration of KC_{8n} (n = 1, 2 and 3) and KC_{12n} (n = 1 and 2). Compared with the standard DFT, DFT-D2 method offers good agreements with the previous experiments and calculations for *c* crystallographic parameters and interlayer distances. The inserted potassium atoms can significantly improve the electronic conductivity of graphite and K-GICs due to those contributions of extra electrons from the inserted potassium atoms making the Fermi levels shift to blue. Two types of potassium point defect (Schottky and Frenkel defect) were investigated and their calculated formation energies are 1.39–2.09 eV and 1.14–1.89 eV, respectively. Potassium ion migrations in the *ab* plane via the vacancy and Frenkel mechanism in K-GICs were researched. The calculated results of migration barrier show that potassium migration via the vacancy mechanism (0.11–1.58 eV) is absolutely prior to that via the Frenkel mechanism (2.42–7.92 eV). Besides, the occupying forms of potassium atoms have significantly influences on the defect properties and potassium migration. Compared with lithium migration in Li-GICs, potassium migration via the vacancy mechanism in K-GICs is more excellent. Thus, K-GICs are promising candidates for anode materials of potassium ion batteries.

1. Introduction

The shortage of Li resources has flogged people to develop other battery technologies for replacing the current lithium-ion batteries, such as sodium-ion batteries (SIBs) and potassium-ion batteries (KIBs) because of the abundant Na, K resources and much lower cost [1–5]. Sodium intercalating into graphite as the negative electrode materials for SIBs is still a great challenge due to the larger size of Na ion compared to the interlayer distance of graphite, as well as higher redox potential of Na/Na^+ (−2.713 V *vs* standard hydrogen electrode). More recently, intense scientific interests have been attracted to potassium-oxygen [6,7], potassium-sulfur [8], Prussian blue [9], and potassium-ion batteries [10–13], which may represent new approaches beyond the current widespread lithium-ion batteries technologies. Pure graphite's failure in NIBs has ever discouraged progress in using graphite as an electrode in KIBs. However, new findings have overturned the science theorem put forward for decades that potassium ions can work with graphite in KIBs. In September 2015, Z. Jian et al., for the first time, reported an electrochemical potassium insertion in graphite, which provides a high reversible capacity of 273 mAh g^{-1} [12]. S. Komaba et al. achieved a highly reversible potassium intercalation into graphite to form the stage-I KC_8 compound with a reversible capacity of 244 mAh g^{-1} at room temperature [11]. W. Luo et al. also pointed that potassium ions can electrochemically intercalate into the graphitic materials, and potassium-graphite intercalation compounds (K-GICs) can deliver a reversible capacity of 207 mAh g^{-1} [13]. All these reported works demonstrate that potassium ions are easier to intercalate into graphite than Na ions in spite of their larger ion size, as depicted in Fig. 1. The stoichiometry of final intercalate compound is KC_8 at room temperature [14], indicating potassium intercalation capacity is higher than sodium.

To date, graphite intercalation compounds (GICs) have been widely investigated as the superconductivity materials, battery

* Corresponding author.
E-mail address: 15216105346@163.com (X. Lv).

http://dx.doi.org/10.1016/j.carbon.2016.06.101
0008-6223/

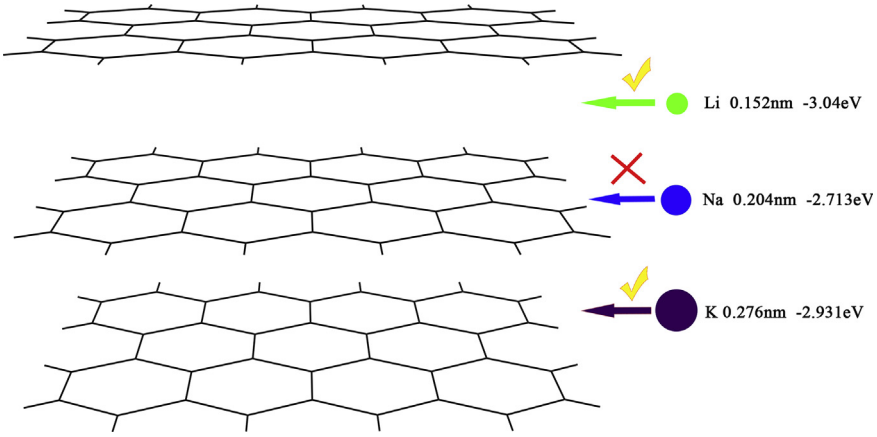

Fig. 1. Schematic illustration of intercalation of Li, Na, and K ions into graphite. Li and K ion can insert into graphite, while Na ion not. (A colour version of this figure can be viewed online.)

electrodes, and catalysts [15,16]. In particular, the most widely known example of GICs is the well-developed Li-GICs for active negative electrodes in LIBs, due to its relatively high lithium intercalation capacity of 372 mAh g^{-1} [17–20]. K. Nobuhara et al. [21–23] have investigated the formation energy and structure of alkali metal-graphite intercalation compounds (AM-GICs) by the AA stacking pattern models. S. Higai et al. [24–27] have studied the adsorption stability of Li atoms on the graphite monolayer surface by first-principles theoretical calculations. C. Hartwigsen et al. [28–31] carried out first-principles electronic structure calculations for AM-GICs of LiC_6 and AMC_8 (AM = Li, Na, K, Rb, and Cs). Furthermore, although K-GICs have been studied by a large number of theoretical calculations [14,29,30], but they mainly focused on the formation energy, adsorption and electronic structure of K-GICs by the standard density functional theory (DFT) method.

To the best of our knowledge, to date, research on the defect chemistry and potassium migration mechanism of K-GICs is quite rare. Moreover, the calculated properties of K-GICs in the published work, such as the *c* lattice parameters, interlayer distances and energies show huge deviations from the experimental data. This is due to that those previous calculations not considering the van der Waals (vdW) interaction between carbon layers, which are not correctly reproduced by the standard DFT. Motivated by this, in this work, the dispersion-corrected density functional theory (DFT-D2) method was employed to calculate the structure, energetics, electronic properties, defect chemistry and cation migration mechanism in KC_{8n} (n = 1, 2 and 3) and KC_{12n} (n = 1 and 2) compounds.

2. Computational methodology

As we all know that the standard DFT gives no correct description for the interlayer van der Waals interaction of layered materials [32–35]. Therefore, our calculations of the structure, energetics, electronic structure, defect chemistry and cation migration in KC_{8n} (n = 1, 2 and 3) and KC_{12n} (n = 1 and 2) were based on the dispersion-corrected density functional theory (DFT-D) [36,37] provided by the CASTEP code [38]. The DFT-D method includes the vdW weak interactions, correcting the tail of the interaction that is missing from PBE. This work used Grimme's DFT-D2 approach [39] to describe the vdW weak interactions between carbon layers. The PBE [40] exchange function in GGA was chosen for calculations and ultrasoft pseudo potentials (USPP) introduced by Vanderbilt [41] have been employed for all the ion-electron interactions. The C $2s^2 2p^2$ electrons and K $3s^2 3p^6 4s^1$ electrons were regarded as the valence electrons. Convergences with respect to both energy cutoff and *k*-point mesh have been carefully tested. Considering the convergence results and the computational efficiency in an integrated manner, an energy cutoff of 500 eV was chosen to ensure the total energies were converged within 1×10^{-4} eV/atom. For the calculations of structure and energy of graphite, $7 \times 7 \times 4$ mesh was carried out by using the Monkhorst-Pack method [42] and the same *k*-point density was used for K-GICs. Whereas for the density of states (DOS) calculations, a denser mesh of $28 \times 28 \times 4$ was used for graphite and we also kept the same *k*-point density for K-GICs.

In order to determine the most-stable configuration of these assumed KC_{8n} (n = 1, 2 and 3) and KC_{12n} (n = 1 and 2) models, atoms and cell optimizations have been performed by using the total energy minimization methods. The total-energy differences were within 10^{-6} eV/atom, the maximum forces were within 0.01 eV/Å, the maximum stresses were within 0.01 GPa and the maximum atom displacements were within 10^{-4} Å. The stabilities of K-GICs were estimated by their formation energies (ΔE). The formation energies were calculated by the following equation [21]: $\Delta E = E_{\text{K-GICs}} - (E_{\text{Graphite}} + E_{\text{K}})$ where $E_{\text{K-GICs}}$, E_{Graphite} and E_{K} is total energy of K-GICs, graphite and K in its pure bulk, respectively. As for the total energy calculations of $E_{\text{K-GIC}}$ and E_{K}, full optimizations of the fractional coordinates and the lattice parameters were also performed by means of the total energy minimization [43]. In addition, the linear synchronous transit/quadratic synchronous transit (LST/QST) combined with the conjugate gradient (CG) method was adopted for the energy barrier calculations of the transition states (TS) and intermediates of potassium ion migration [44]. A maximum energy pathway was obtained by the LST method along the path between the reactant and product, and TS approximation was constructed from the pathway by the QST maximization. Then CG minimization was performed. The stationary point along this path was a real transition state, which was located by cycles of the QST maximization with CG refinement until the convergence was obtained or the maximum number of allowed QST steps was reached. Finally, TS confirmations were conducted by the nudged elastic band (NEB) method [45].

3. Results and discussions

3.1. Structure and stability

After full geometrical optimizations, the most-stable structures were obtained, as shown in Fig. 2. In general, alkali metal density has an important influence on the stage structure of AM-GICs, and

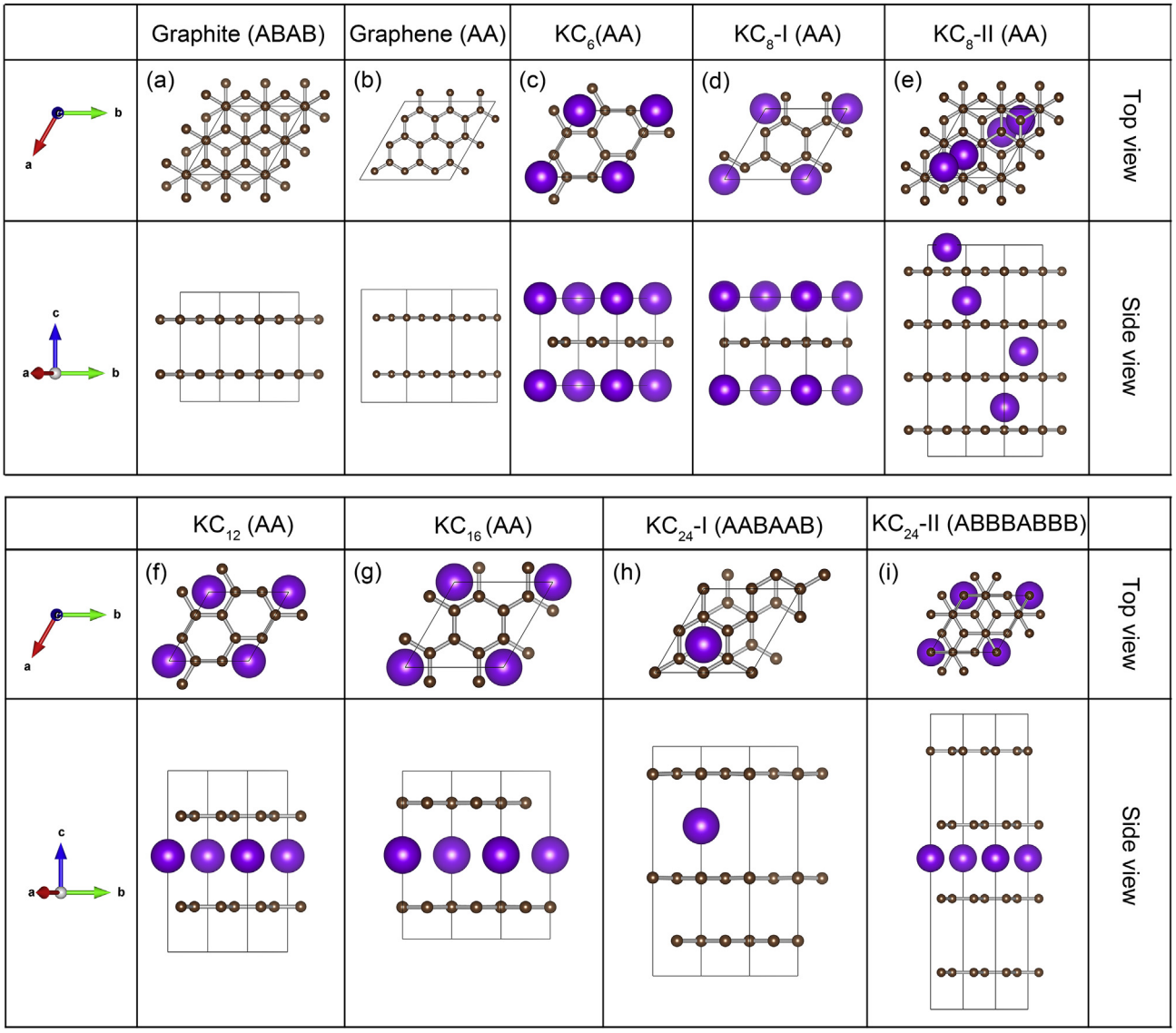

Fig. 2. Top and side views, carbon layers stacking sequences of calculated hexagonal cells of (a) graphite, (b) graphene, (c) KC_6, (d) KC_8-I, (e) KC_8-II, (f) KC_{12}, (g) KC_{16}, (h) KC_{24}-I and (i) KC_{24}-II. The purple and black balls represent K and C atoms, respectively. (A colour version of this figure can be viewed online.)

alkali metal density was considered to decrease by changing from 1st to higher stage structure. The nth stage AM-GICs (e.g. nth stage K-GICs $[(KC_8)(C_8)_{n-1}$, n = 1, 2 and 3]) is composed of the graphene layers occupied by alkali metal with the possible highest density (e.g. KC_8) and (n−1) empty graphene layers $[(C_8)_{n-1}]$, as shown in Fig. 2. The carbon layers of graphite are in the ABAB stacking pattern (Fig. 2a), whose stage index $n \rightarrow \infty$. On one hand, for KC_{8n} (n = 1, 2 and 3), potassium atoms form a 2D hexagonal $p(2 \times 2)$ unit cell, and occupy those sites between carbon layers above the centers of carbon hexagons. Carbon layers and potassium atoms of KC_8 all stack as the AA pattern (stage-I, Fig. 2d), named as KC_8-I. Moreover, potassium atoms of KC_8 in the out-of-plane direction and the corresponding carbon layers have a stacking sequence of AαAβAγAδ, named as KC_8-II (Fig. 2e). Carbon layers of KC_{16} (stage-II) are in the AA stacking sequence (Fig. 2g), while the AABAAB stacking pattern is only for carbon layers of KC_{24}-I (stage-III) (Fig. 2h). On the other hand, KC_{12n} (n = 1 and 2) were also considered in this work, where potassium atoms form a 2D hexagonal $p(\sqrt{3} \times \sqrt{3})$-R30° unit cell. As shown in Fig. 2f, carbon layers of KC_{12} (stage-II) are also in the AA stacking sequence, while in KC_{24} (stage-IV) carbon layers stack as a sequence of ABBBABBB (Fig. 2i), called as KC_{24}-II.

The calculations of structure parameters, such as lattice parameters *a* and *c*, carbon layer (near potassium atoms) and C-C (K) interatomic bond lengths for graphite, KC_{8n} (n = 1, 2 and 3) and KC_{12n} (n = 1 and 2) were carried out by fully relaxing their atoms and cells. To test the accuracy of the standard DFT method, the PBE exchange function was employed for comparison with the dispersion correction (DFT-D2). The calculated structure parameters in comparison with the experimental results are listed in Table 1. In general, lattice parameter *c* of graphite is sensitive to the weak vdW interactions between carbon layers, so it can measure the accuracy of our calculations by DFT-D2. Seen from Table 1, the standard DFT method apparently overestimates *c* lattice parameters for graphite (by 36%) and KC_8-I, KC_8-II, KC_{16} and KC_{24}-I (with an absolute deviation of 0.4, 0.38, 0.59 and 1.08 Å, respectively) compared to the experimental values [46] and theoretical calculations by vdW-DF2 [13]. In addition, DFT in combination with the dispersion corrected method makes *c* parameters of KC_8-I, KC_8-II, KC_{16} and KC_{24}-I agree well with the experiments and previous theoretical calculations,

Table 1
Comparisons of calculated lattice parameters (*a* and *c* in Å) with experimental and theoretical values for graphite, KC_{8n} (n = 1, 2 and 3) and KC_{12n} (n = 1 and 2).

	a_{PBE}	a_{DFT-D2}	a_{Exp}	c_{PBE}	c_{DFT-D2}	c_{Exp}
Grahpite	2.4573	2.4572	2.46[a], 2.47[e]	9.2203	6.8529	6.77[b]
KC_8-I	4.9459	4.9443	4.96[c], 4.97[e]	5.9341	5.5143	5.53[d],5.53[e]
KC_8-II	4.9643	4.9585	4.96[f]	21.7806	21.4360	21.40[g]
KC_{12}	4.2873	4.2863		11.1081	10.5994	
KC_{16}	4.9420	4.9440	4.96[e]	9.67120	8.8530	9.09[e]
KC_{24}-I	4.9294	4.9297	4.95[e]	13.7157	12.0763	12.63[e]
KC_{24}-II	4.2771	4.2699		18.0796	14.9393	

[a] Ref. [14].
[b] Ref. [46].
[c] Ref. [47].
[d] Ref. [48].
[e] Ref. of calculation [13].
[f] Ref. [49].
[g] Ref. [50].

with an absolute deviation of 0.12, 0.07, 0.24 and 0.54 Å, respectively. The calculated *a* lattice parameters of graphite, KC_8-I, KC_8-II, KC_{16} and KC_{24}-I are in good agreements with the experimental values by both PBE and DFT-D2 methods, generally with an absolute deviation of 0.02 Å, indicating that PBE is fully competent in describing the covalent interactions between carbon atoms.

Moreover, it is found that the calculated *c* lattice parameters of K-GICs with higher potassium concentration by the standard DFT method were more close to that calculated by the dispersion corrections (DFT-D2) method. It may be caused by two reasons: on one hand, vdW interactions among the carbon layers compete with the attractive interactions between potassium and carbon atoms. On the other hand, more alkali metal atoms can screen a part of weak vdW interactions. Therefore, what is certain is that the concentration of inserted potassium atoms plays a significant role in the stability for K-GICs, and K-GICs with more potassium inserted exhibits more hard characteristic than graphite.

The calculated carbon layer (contain potassium atom) distances and C-C (K) interatomic distances compared to the experimental data are listed in Table 2. In all cases, the deviations for carbon layer distances between our calculated results by the DFT-D2 method and experimental values don't exceed 0.03 Å. For C-C and C-K bond length, the calculated results are in fairly good agreements with the experiments, and the corresponding deviations are generally within 0.01 Å. In 2013, J C. Chacon-Torres et al. reported the Raman spectroscopy analysis of potassium graphite intercalation compounds and pointed that C-C bond length slightly increases with the increase of potassium concentration [51], and our calculated C-C bond lengths of KC_{8n} (n = 1, 2 and 3) and KC_{12n} (n = 1, and 2) also obey this tendency. Interestingly, with the increase of potassium concentration in KC_{8n} (n = 1, 2 and 3), all carbon layer distances and

Table 2
Comparisons of calculated (DFT-D2) carbon layer distances and C-C (K) interatomic distances (in Å) for graphite, KC_{8n} (n = 1, 2 and 3) and KC_{12n} (n = 1 and 2) system.

	d^{L}_{Cal}	d^{L}_{Exp}	d^{C-C}_{Cal}	d^{C-C}_{Exp}	d^{K-C}_{Cal}	d^{K-C}_{Exp}
Grahpite	3.4920	3.39[a], 3.50[c]	1.4187	1.42[a]		
KC_8-I	5.5143	5.53[b], 5.53[c]	1.4293	1.44[b],1.44[c]	3.1056	3.12[b], 3.11[c]
KC_8-II	5.6090		1.4332		3.1494	
KC_{12}	5.3530	5.32[d]	1.4287	1.43[d]	3.0339	3.02[d]
KC_{16}	5.5997	5.62[c]	1.4272	1.43[c]	3.1426	3.15[c]
KC_{24}-I	5.6512	5.66[c]	1.4231	1.43[c]	3.1637	3.17[c]
KC_{24}-II	5.2960		1.4233		3.0063	

[a] Ref. [46].
[b] Ref. [14].
[c] Ref. of calculation [13].
[d] Ref. of calculation [21].

Table 3
Comparisons of calculated formation energies (in eV) for KC_6, KC_{8n} (n = 1, 2 and 3) and KC_{12n} (n = 1 and 2).

	KC_6	KC_8-I	KC_8-II	KC_{12}	KC_{16}	KC_{24}-I	KC_{24}-II
PBE	0.38	−0.51	−0.68	0.26	−0.47	−0.33	−0.02
DFT-D2	0.09	−1.54	−1.81	−1.10	−2.53	−3.83	−3.39
Ref		−0.51[a], −0.50[c]	−1.24[b]	−0.38[c]	−0.60[c]		

[a] Calculated value with PBE method in Ref. [14].
[b] Experimental value in Ref. [53].
[c] Calculated values with PBE method in Ref. [21].

C-K bond length shrink. This is contrary to the rule in LiC_n (n = 6,12), as reported in previous literature [31], and it may be due to the attractive interactions between C atom and K ion are stronger than that between C atom and Li ion. Moreover, KC_{12n} (n = 1 and 2) also exhibits this inverse tendency.

Table 3 lists the calculated formation energy results of KC_6, KC_{8n} (n = 1, 2 and 3) and KC_{12n} (n = 1 and 2) compared to the experiments. The calculated value of −0.51 eV by PBE for KC_8-I is in fairly good agreement with the results of −0.51 and −0.5 eV by PBE from literature [14,21]. The formation energy by experiment of KC_8-II at 550 K is −1.24 eV, whose potassium atoms and carbon layers in the out-of-plane direction also have a stacking sequence of AαAβAγAδ. Our calculated result of −1.81 eV for KC_8-II by DFT-D2 has a significantly difference from the experimental result, with an absolute deviation of nearly 0.6 eV. It may be associated with the fact that the graphite reference system is not stable enough at the DFT level compared to AM-GICs [31] and our DFT calculations are based on 0 K rather than 550 K in experiments. What's more, the calculated formation energy for KC_8-II is lower than the results of KC_8-I both by PBE and DFT-D2, indicating carbon layers and potassium atoms in KC_8-II stacking as a sequence of AαAβAγAδ in the out-of-plane direction is more thermodynamic stable than KC_8-I whose potassium atoms stacking as a αα sequence. For the formation energy of KC_{24}, KC_{24}-I is slightly lower than KC_{24}-II, it may be because potassium ions with an occupying form of 2D hexagonal $p(\sqrt{3} \times \sqrt{3})$ -R30° sites in KC_{24}-II have larger Coulomb repulsion interactions than KC_{24}-I with an occupying form of 2D hexagonal $p(2 \times 2)$.

With the increase of K/C ratio, the calculated formation energy by DFT-D2 increases accordingly, which indicates that inserting more potassium atoms into graphite with many advance potassium storage is difficult than that with few advance potassium storage. It is clear that the strong Coulomb repulsive interactions among potassium atoms beat the weak vdW forces between carbon layers and reduce the stability of K-GICs. This tendency of K-GICs is consistent with that of Li-GICs [31]. However, the calculated formation energies by PBE are some chaotic and higher than that calculated by DFT-D2. Especially for these K-GICs with low concentration of alkali metal, the significant weak vdW forces are not well described, hence PBE is unsatisfactory in describing the formation energies for AM-GICs materials. To confirm our calculation results of KC_{8n} (n = 1, 2 and 3) and KC_{12n} (n = 1 and 2), another important formation energy of KC_6 (Fig. 2c) was carefully calculated. The positive results of 0.38 eV by PBE and 0.09 eV by DFT-D2 indicate that KC_6 is not thermodynamically stable, which is consisted with the reported results from literature [14,29,52]. It reveals that our above formation energy calculations for K-GICs at the DFT-D2 level are reasonable and believable.

3.2. Electronic structure

The electronic transport is an important factor that determines the rate capability of the anode materials in KIBs, therefore, the

projected density of states (DOS) in a window of ± 5 eV around the Fermi level of KC_{8n} (n = 1, 2 and 3) and KC_{12n} (n = 1 and 2) were calculated and compared to graphite, as depicted in Fig. 3. Viewed from Fig. 3a, graphite has a lower DOS around the Fermi level (E_F = 0 eV, dotted line in Fig. 3a) and metallic characters. Indeed, there is an electron-hole symmetry around the Fermi energy in graphite and the Fermi level is a "local valley" between occupied and unoccupied states. The width of calculated valence band (VB) for graphite is nearly 20 eV, which is in good agreement with the experimental value of 21 eV by X-ray photoemission spectra [54]. Its VB is composed of C-2*s* and C-2*p* orbitals, in which 2*s* orbitals dominate the lower-energy levels from −20 to −10 eV, while 2*p* orbitals dominate the higher-energy levels from −10 eV to the Fermi level.

In the case of K-GICs, the presence of potassium has a significant impact on the distributions of electron quantum states (Fig. 3b–g). For example, the Fermi level of KC_8-I shifts to blue (about 2 eV) due to the contributions of extra electrons from the inserted potassium. These extra electrons give rise to a larger DOS near the Fermi level compared to graphite. Making comparisons among Fig. 3c–f, it is found that the electron states around the Fermi level of K-GICs are positively associated with the potassium concentration. Therefore, K-GICs are not only keeping the metallic characters with continuous DOS around their Fermi levels, but also the inserted potassium can improve the electronic conductivity of graphite and K-GICs. For two phases of KC_8, the electron states around the Fermi level of KC_8-I are slightly more than that of KC_8-II, which means that under the same potassium concentration, the electronic conductivity of KC_8-I is superior to KC_8-II by a little.

In addition, seen from Fig. S2a–f in Supporting information, the conduction band (CB) width of KC_8-I shrinks to 14 eV compared to 21 eV of graphite, and other K-GICs approximately shrink to 7 eV. All these PDOS show that the 3*p* orbitals of intercalated K atoms are localized at the low energy levels (at about −16 eV) of VB. Unlike graphite, the VBs of K-GICs are dominated by the 3*p* orbitals of potassium atoms and 2*p* orbitals of carbon atoms. Meanwhile, the charge difference map of KC_8-II was plotted in Fig. 4. From it, the ionic characters of potassium can be clearly observed, verifying the main interactions between potassium and carbon layers are ionic. Electrons located between two carbon atoms were found, which demonstrates the C-C bonds are covalent.

3.3. Defect properties

Given Schottky defect and Frenkel defect are the intrinsic characteristics due to the lattice vibrations. In this section, two types of defect, potassium atom Schottky defect and Frenkel defect were examined. To prepare initial structures for the defective system, full optimizations for atomic fractional coordinates of non-defective supercell were carried out at the DFT-D2 level. In order to simulate the Schottky defect with low concentration vacancy, one potassium atom was removed from a 2 × 2 × 1 supercell of KC_8-I, KC_8-II, KC_{12}, KC_{16}, KC_{24}-I and KC_{24}-II, respectively, as shown in Fig. 5. Subsequently, these defective geometries were fully optimized without any symmetry constraints. The formation energy $E_{De}[S]$ of one potassium Schottky defect was calculated by the following equation: $E_{De}[S] = E_S[S] + E[K] - E_S$, here, $E_S[S]$ and E_S was the total energy at DFT-D2 level of the optimized supercell structure with and without potassium atom vacancy, respectively, and $E[K]$ was the energy of a single potassium atom.

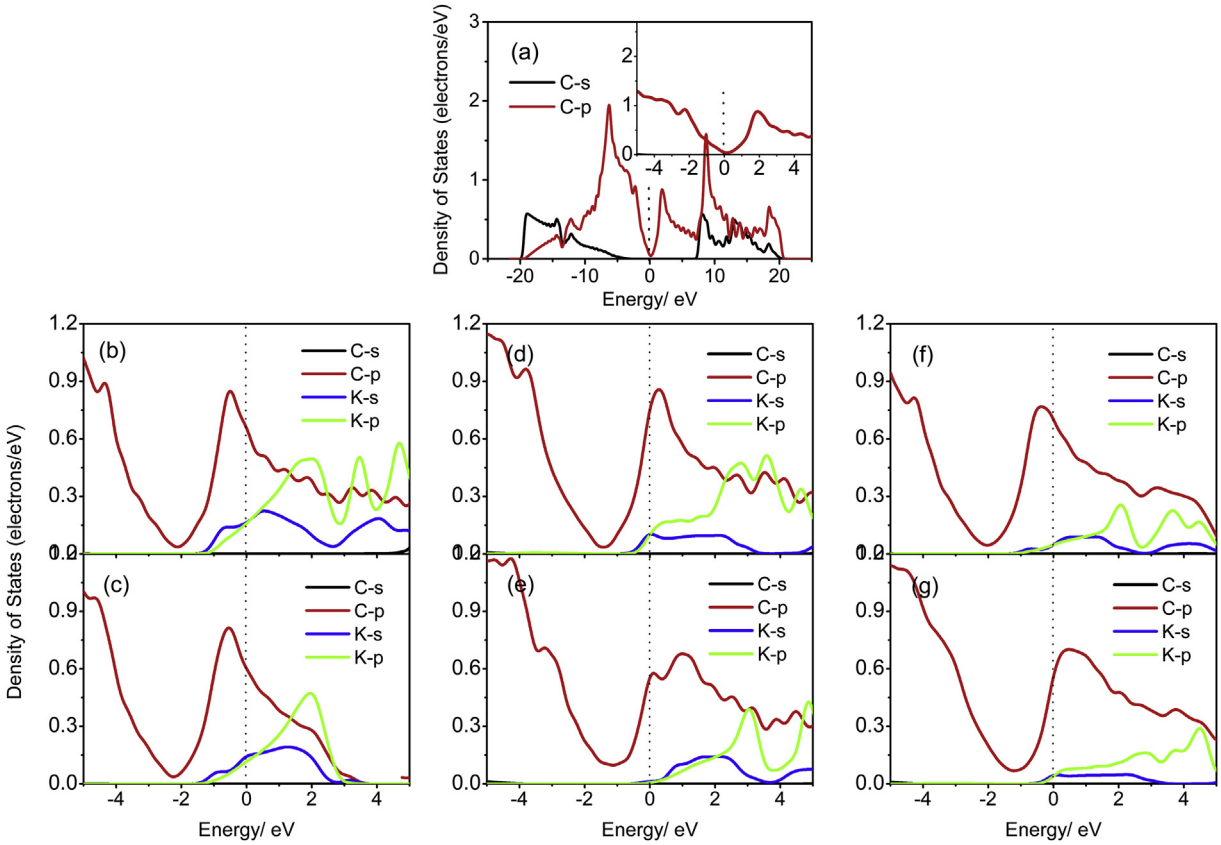

Fig. 3. Projected density of states (PDOS) in a window of ± 5 eV around the Fermi level of (a) graphite, (b) KC_8-I, (c) KC_8-II, (d) KC_{12}, (e) KC_{16}, (f) KC_{24}-I and (g) KC_{24}-II, respectively. Fermi energy level was set to zero (dotted line). (A colour version of this figure can be viewed online.)

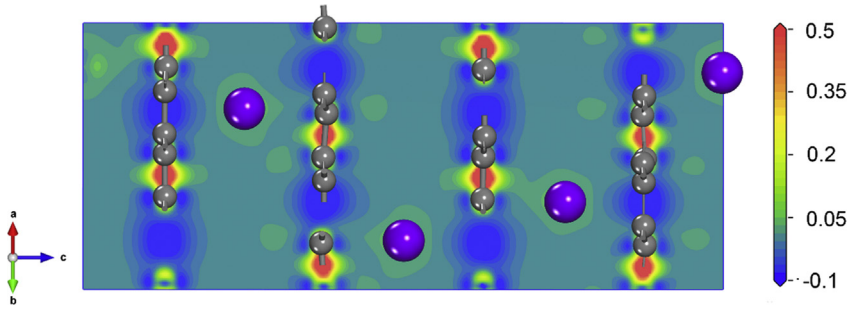

Fig. 4. Charge difference plot of KC_8-II, the red and blue areas represent electron gains and loses (unit: electrons/Å^3). (A colour version of this figure can be viewed online.)

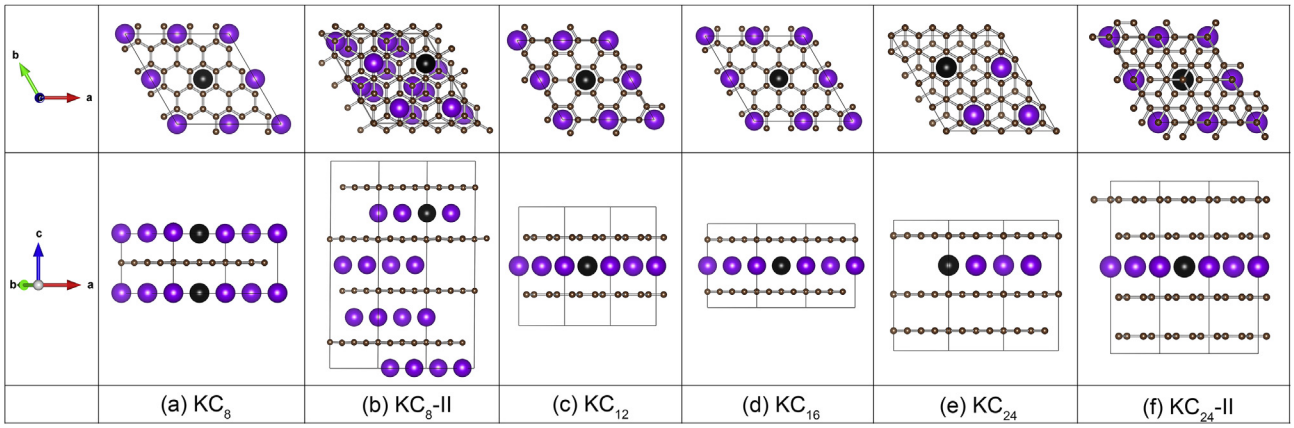

Fig. 5. Schematic representations of 2 × 2 × 1 supercell with low concentration vacancy point defect (black site) of K-GICs. (A colour version of this figure can be viewed online.)

The calculated defect formation energy of one potassium atom Schottky defect is 1.78, 2.09, 1.41, 1.87, 2.07 and 1.39 eV/supercell of KC_8-I, KC_8-II, KC_{12}, KC_{16}, KC_{24}-I and KC_{24}-II, respectively, as listed in Table 4. These Schottky defect formation energies are all positive, implying that forming a vacancy defect needs to absorb some energy. Usually, a single atom is in the state of thermal motion with a kinetic energy about 0.03 eV at room temperature, which is much less than the formation energy of one potassium atom Schottky defect in a 2 × 2 × 1 K-GICs supercell. Therefore, the concentration of vacancy defect in real K-GICs is small under the normal operating conditions. For KC_{8n} (n = 1, 2 and 3) with the same potassium atom occupying form of 2D $p(2 \times 2)$ hexagonal, with the increase of potassium concentration, the formation energies of one potassium atom vacancy defect in the 2 × 2 × 1 K-GICs supercell reduce, it may be due to the reason that more repulsive interactions of potassium ions making it easy to form a potassium vacancy. For KC_{12n} (n = 1 and 2) with the same potassium atom occupying form of 2D $p(\sqrt{3} \times \sqrt{3})$ hexagonal, the formation energies are similar (1.41 eV of KC_{12} *vs* 1.39 eV of KC_{24}-II). Moreover, the stacking sequence and occupying form of potassium atoms in KC_8 and KC_{24} have significantly influence on the formation energy of potassium vacancy defect in the 2 × 2 × 1 K-GICs supercell.

A Frenkel defect is a vacancy-interstitial pair forming when an atom jumps from a normal lattice point to an interstitial site. To establish a Frenkel defect, a potassium atom was undocked from its original position to form a vacancy site (black site) and was subsequently placed at an interstitial site (red site) in the 2 × 2 × 1 supercell of KC_8-I, KC_8-II, KC_{12}, KC_{16}, KC_{24}-I and KC_{24}-II (as respectively shown in Fig. 6). Here, the interstitial sites of these K-GICs are adjacent to the vacancy sites in the same carbon layer plane, while those interstitial sites in another new vacant carbon layer are impossible because of the ion radius (1.7 Å) of potassium is much larger than the radius of carbon hexagonal hollow (about 1.45 Å).

Table 4
Calculated formation energies (in eV/supercell) of a potassium Schottky defect $E_{De}[S]$ and a potassium Frenkel defect $E_{De}[Fr]$.

	KC_8-I	KC_8-II	KC_{12}	KC_{16}	KC_{24}-I	KC_{24}-II
$E_{De}[S]$	1.78	2.09	1.41	1.87	2.07	1.39
$E_{De}[Fr]$	1.30	1.43	1.89	1.14	1.30	1.76

The formation energies of potassium Frenkel defects $E_{De}[Fr]$ were calculated according to the following equation: $E_{De}[Fr] = E_F[Fr] - E_F$, where $E_F[Fr]$ and E_F is the total energy at the DFT-D2 level of the optimized supercell structure with and without potassium atom Frenkel defects, respectively. The calculated results of formation energy of potassium Frenkel defect are summarized in Table 4. It is can be seen that the Frenkel formation energy of KC_{24}-I is same as KC_8-I. Interestingly, the energy needed to form a potassium atom Frenkel defect in KC_{8n} (n = 1, 2 and 3) is smaller than that to form a potassium vacancy defect, while all the formation energies of one potassium atom Frenkel defect are higher than that of one Schottky defect in KC_{12n} (n = 1 and 2), indicating the occupying form of potassium atom in KC_{8n} (n = 1, 2 and 3) and KC_{12n} (n = 1 and 2) has an important effect on the main type of defect in K-GICs. The reason can be attributed to that the Coulomb repulsion interactions between potassium atoms in the occupying form of $p(\sqrt{3} \times \sqrt{3})$ hexagonal are larger than that of $p(2 \times 2)$ hexagonal.

3.4. Potassium ion migration

A good rate capability is significant requirement for a promising

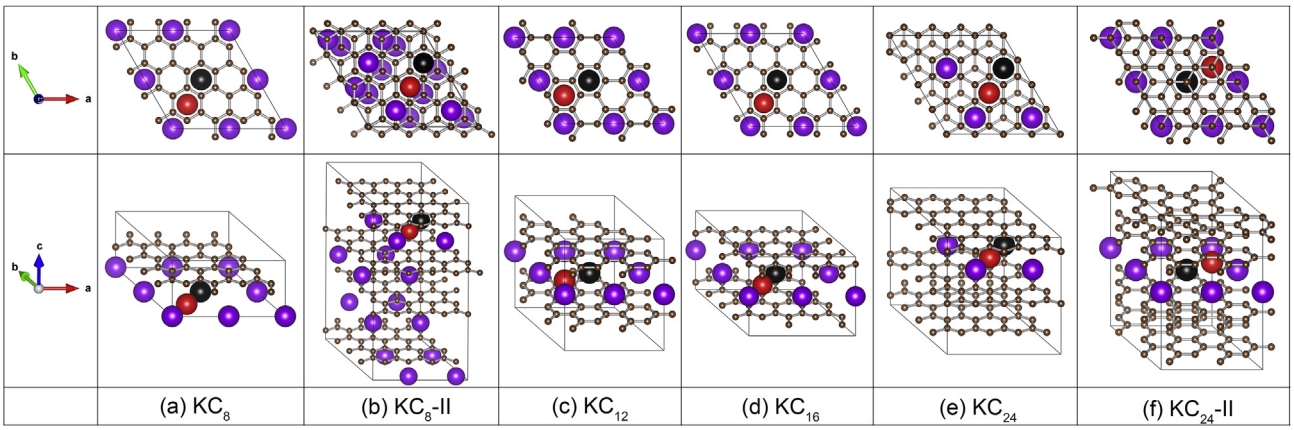

Fig. 6. Schematic representations of 2 × 2 × 1 supercell with low concentration Frenkel defect of K-GICs; interstitial sites in red and corresponding vacancy in black. (A colour version of this figure can be viewed online.)

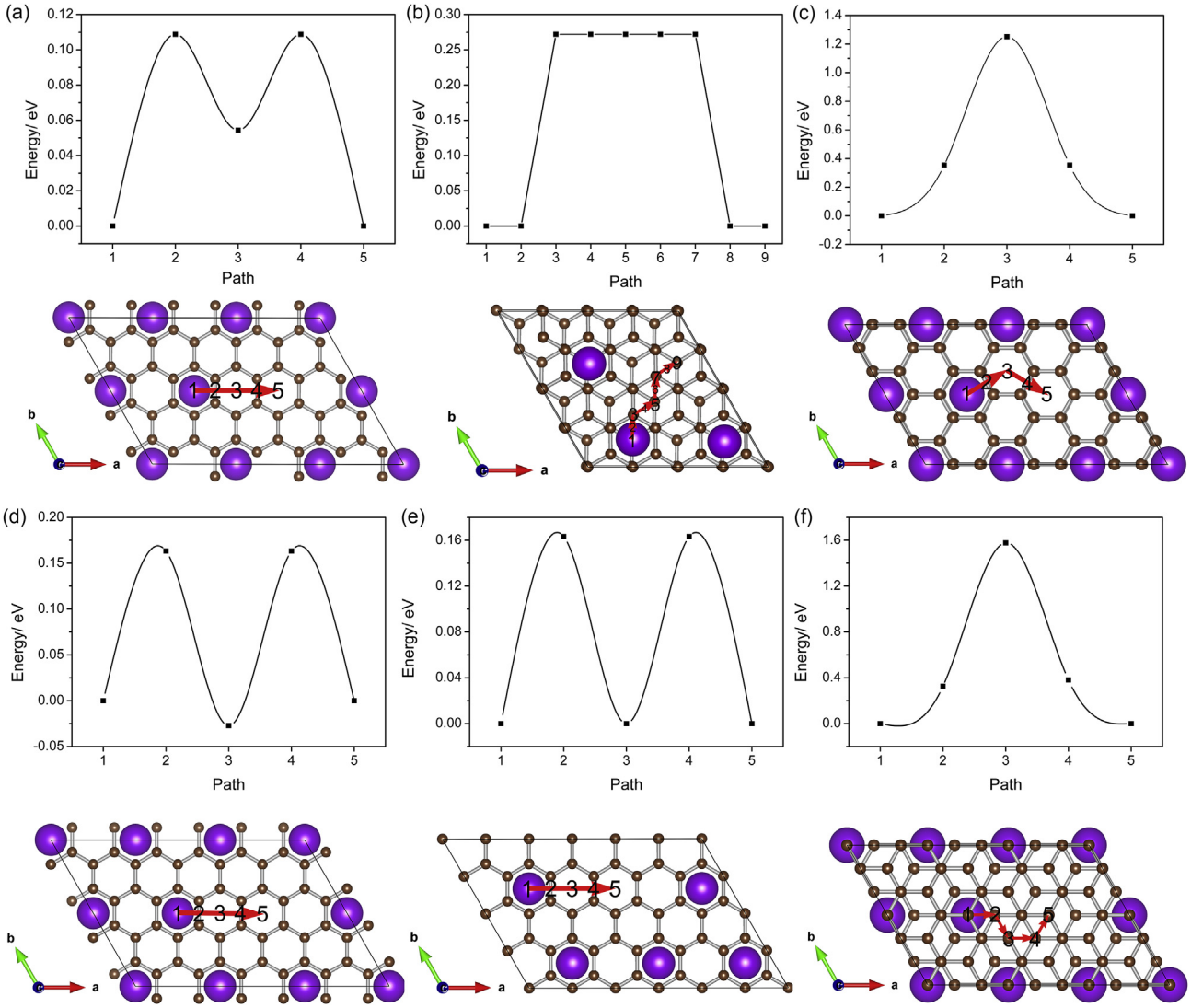

Fig. 7. Potential energy curves and graphic patterns of pathway A via vacancy mechanism of (a) KC_8-I, (b) KC_8-II, (c) KC_{12}, (d) KC_{16}, (e) KC_{24}-I and (f) KC_{24}-II. (A colour version of this figure can be viewed online.)

anode material for KIBs, especially in high power density applications. It is known that the rate capability is mainly dependent on the transport properties of potassium ion and electron, corresponding to the potassium migration barrier and electronic conductivity of K-GICs. In section 3.2, we found the inserted potassium atoms can enhance the electronic conductivity of graphite and K-GICs. Thus, in this section the potassium ion migration processes were investigated and discussed.

Generally, potassium ion migration in KC_{8n} (n = 1, 2 and 3) and KC_{12n} (n = 1 and 2) mainly involves two defect mechanisms discussed in Section 3.3: (i) the vacancy mechanism of potassium diffusion via a Schottky defect and (ii) the Frenkel migration mechanism where potassium migrates through a potassium Frenkel defect. In this work, only potassium diffusions along the *ab* plane were studied. Potassium diffusion along the crystallographic *c* direction was not considered, because it is kinetically prohibited for potassium to migrate through the carbon hexagonal hollows.

Potassium migrations along the crystallographic *ab* plane in KC_{8n} (n = 1, 2 and 3) and KC_{12n} (n = 1 and 2) were researched along two most-possible migration pathways: (i) migration pathway A where potassium passes through a carbon hexagon to the adjacent vacancy site, as depicted in Fig. 7; and (ii) migration pathway B where potassium firstly moves to the adjacent carbon hexagon (B-I) then turns to the vacant channels (B-II and III), as depicted in Fig. 8. For all the considered K-GICs, the pathway A involves the vacancy mechanism where potassium ion migrates from its regular position to a potassium vacancy site. While the Frenkel mechanism is only possible for the B migration pathway due to the vacant channels in this pathway can provide essential interstitial sites for potassium.

Fig. 7 shows the potential energy curves and graphic patterns of pathway A via the vacancy mechanism for KC_{8n} (n = 1, 2 and 3) and KC_{12n} (n = 1 and 2). It can be seen that, in the cases of KC_{8n} (n = 1, 2 and 3) with the same potassium atom occupying form of $p(2 \times 2)$ hexagonal, potassium goes straightly through two transition states via the vacancy mechanism. While for cases of potassium migration via the vacancy mechanism in KC_8-II and KC_{12n} (n = 1 and 2), only one transition state was observed due to their more compact potassium occupying form of $p(\sqrt{3} \times \sqrt{3})$ hexagonal.

The calculated E_a values of potassium migration in KC_{8n} (n = 1, 2 and 3) and KC_{12n} (n = 1 and 2) through path A via the vacancy mechanism are listed in Table 5. From it, the energy barriers of potassium migration via the vacancy mechanism in KC_{8n} (n = 1, 2 and 3) with potassium atom occupying form of $p(2 \times 2)$ hexagonal are all smaller (0.11–0.27 eV) than that 1.25–1.58 eV of KC_{12n} (n = 1

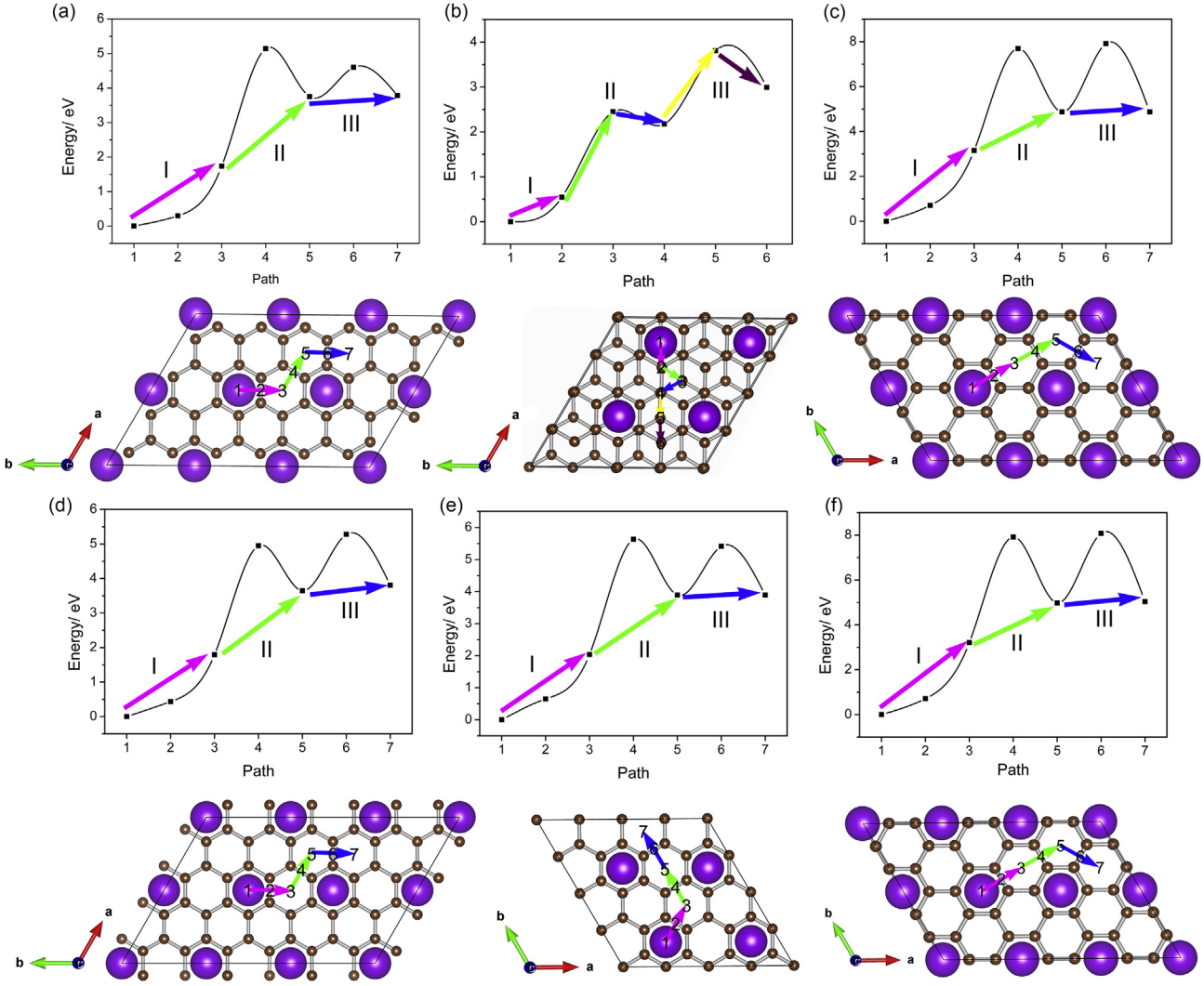

Fig. 8. Potential energy curves and graphic patterns of pathway B via Frenkel defect mechanism of (a) KC_8-I, (b) KC_8-II, (c) KC_{12}, (d) KC_{16}, (e) KC_{24}-I and (f) KC_{24}-II. (A colour version of this figure can be viewed online.)

Table 5
Calculated energy barriers E_a (in eV) of potassium migration by vacancy mechanism and Frenkel mechanism along the crystallographic *ab* plane in KC_{8n} (n = 1, 2 and 3) and KC_{12n} (n = 1 and 2).

	KC_8-I	KC_8-II	KC_{12}	KC_{16}	KC_{24}-I	KC_{24}-II
Path A	0.11	0.27	1.25	0.16	0.16	1.58
Path B-II	3.40	1.90	4.54	3.16	3.59	4.71
Path B-III	0.84	1.63	3.05	1.63	1.52	3.10

and 2), which means the potassium atom occupying form has a significant effect on potassium migration. In addition, for KC_8-I, the saddle point is located at 0.05 eV, while 0 eV and −0.03 eV for KC_{24}-I and KC_{16}, respectively. This is the result of that, for KC_{24}-I and KC_{16}, potassium ions migrate via the vacancy mechanism to those intermediate sites, whose potentials are equal to the starting sites even lower than those due to their structural symmetry.

The potential energy curves and graphic patterns of potassium migration via the Frenkel defect (path B) depicted in Fig. 8 show that the migration process of path B is mainly divide into three steps (I, II and III). In step I, potassium migrates to the higher potential site of the adjacent carbon hexagonal, which consumes 1.74, 0.54, 3.16, 1.8, 2.04 and 3.21 eV of KC_8-I, KC_8-II, KC_{12}, KC_{16}, KC_{24}-I and KC_{24}-II, respectively. Then potassium turns to the vacant channel and migrates by striding an energy barrier of 3.40, 1.90, 4.54, 3.16, 3.59 and 4.71 eV (in Table 5) for KC_8-I, KC_8-II, KC_{12}, KC_{16}, KC_{24}-I and KC_{24}-II, respectively, and this process is called as step II. In the following migration process of step III, the activation energy for potassium migration reduces to 0.84, 1.63, 3.05, 1.63, 1.52 and 3.10 eV for KC_8-I, KC_8-II, KC_{12}, KC_{16}, KC_{24}-I and KC_{24}-II, respectively. Therefore, respectively for KC_8-I, KC_8-II, KC_{12}, KC_{16}, KC_{24}-I and KC_{24}-II, an energy of 5.14, 2.45, 7.7, 4.95, 5.63 and 7.92 eV is need to finish the whole migration processes of path B via the Frenkel defect mechanism. Among them, a relatively small energy barrier of 2.45 eV for KC_8-II was observed, indicating potassium migration via the Frenkel defect mechanism in KC_8-II is more preferential than other K-GICs.

Making comparisons among two migration mechanisms, an important observation is that, potassium migration via the vacancy mechanism is intensively favorable than the Frenkel mechanism with higher energy barriers. More interestingly, all the activation energies for potassium migration via the vacancy mechanism are dramatically lower than that Li ion in Li-GICs (0.42–0.56 eV) [31], indicating the migration ability of potassium in K-GICs is more excellent than Li in Li-GICs. All above evidences demonstrate that applying K-GICs as anode materials for potassium-ion batteries is absolutely feasible with a high speed of charge and discharge.

4. Conclusions

The structure, energetics, electronic structure, defect properties and cation migration in KC_{8n} (n = 1, 2 and 3) and KC_{12n} (n = 1 and 2) were investigated theoretically with the dispersion-corrected DFT-D2 method. DFT-D2 offers good agreement with the previous experiments and calculations for the *c* crystallographic parameters and interlayer distances compared to the standard DFT. The inserted potassium can improve the electronic conductivity of graphite due to the contribution of extra electrons from potassium atoms making the Fermi level shift to blue. Two kinds of point defect, potassium Schottky (S_K) and Frenkel (F_K) defect were investigated. The calculated formation energies for E_S and E_F are 1.39–2.09 eV and 1.14–1.89 eV, respectively. Potassium migration in the *ab* plane via the vacancy and Frenkel mechanism in KC_{8n} (n = 1, 2 and 3) and KC_{12n} (n = 1 and 2) compounds were researched. The calculated activation barriers of potassium migration in the *ab* plane show that potassium migration via the vacancy Schottky mechanism (0.11–1.58 eV) is absolutely preferential compared to that via the Frenkel mechanism (2.42–7.92 eV). Furthermore, the occupying form of potassium atom has a significantly influence on the defect properties and potassium migration. Potassium migration via the vacancy mechanism in K-GICs is more excellent than lithium migration in Li-GICs. All calculated results demonstrate that K-GICs are promising candidates for potassium-ion battery anode materials.

Acknowledgments

We sincerely acknowledge the High Performance Computing Center of CSU, China. This work was financially supported by the National Science and Technology Support Project of China (No. 2012BAE08B02).

Appendix A. Supplementary data

Supplementary data related to this article can be found at http://dx.doi.org/10.1016/j.carbon.2016.06.101.

References

[1] S.-W. Kim, D.-H. Seo, X. Ma, G. Ceder, K. Kang, Electrode materials for rechargeable sodium-ion batteries: potential alternatives to current lithium-ion batteries, Adv. Energy Mater. 2 (7) (2012) 710–721.
[2] M.D. Slater, D. Kim, E. Lee, C.S. Johnson, Sodium-ion batteries, Adv. Funct. Mater 23 (8) (2013) 947–958.
[3] Y. Qi, L. Mu, J. Zhao, Y.S. Hu, H. Liu, S. Dai, Superior Na-storage performance of low-temperature-synthesized $Na_3(VO_{(1-x)}PO_4)_2F_{(1+2x)}$ $(0</=x</=1)$ nanoparticles for Na-ion batteries, Angew. Chem. Int. Ed. Engl. 54 (34) (2015) 9911–9916.
[4] L. Wang, Y. Lu, J. Liu, M. Xu, J. Cheng, D. Zhang, J.B. Goodenough, A superior low-cost cathode for a Na-ion battery, Angew. Chem. Int. Ed. Engl. 52 (7) (2013) 1964–1967.
[5] Z. Xu, X. Lv, J. Li, J. Chen, Q. Liu, A promising anode material for sodium-ion battery with high capacity and high diffusion ability: graphyne and graphdiyne, RSC Adv. 6 (2016) 25594–25600.
[6] Xiaodi Ren, Yiying Wu, A low-overpotential potassium-oxygen battery based on potassium superoxide, J. Am. Chem. Soc. 135 (8) (2013) 2923–2926.
[7] W.D. McCulloch, X. Ren, M. Yu, Z. Huang, Y. Wu, Potassium-ion oxygen battery based on a high capacity antimony anode, ACS Appl. Mater. Interfaces 7 (47) (2015) 26158–26166.
[8] Q. Zhao, Y. Hu, K. Zhang, J. Chen, Potassium-sulfur batteries: a new member of room-temperature rechargeable metal-sulfur batteries, Inorg. Chem. 53 (17) (2014) 9000–9005.
[9] C.D. Wessells, S.V. Peddada, R.A. Huggins, Y. Cui, Nickel hexacyanoferrate nanoparticle electrodes for aqueous sodium and potassium ion batteries, Nano Lett. 11 (12) (2011) 5421–5425.
[10] Zelang Jian, Zhenyu Xing, Clement Bommier, Zhifei Li, X. Ji, Hard carbon microspheres: potassium-ion anode versus sodium-ion anode, Adv. Energy Mater. 6 (3) (2016) 1501874, http://dx.doi.org/10.1002/aenm.201501874.
[11] S. Komaba, T. Hasegawa, M. Dahbi, K. Kubota, Potassium intercalation into graphite to realize high-voltage/high-power potassium-ion batteries and potassium-ion capacitors, Electrochem. Commun. 60 (2015) 172–175.
[12] Z. Jian, W. Luo, X. Ji, Carbon electrodes for K-ion batteries, J. Am. Chem. Soc. 137 (36) (2015) 11566–11569.
[13] W. Luo, J. Wan, B. Ozdemir, W. Bao, Y. Chen, J. Dai, H. Lin, Y. Xu, F. Gu, V. Barone, L. Hu, Potassium ion batteries with graphitic materials, Nano Lett. 15 (11) (2015) 7671–7677.
[14] E. Ziambaras, J. Kleis, E. Schröder, P. Hyldgaard, Potassium intercalation in graphite: a van der Waals density-functional study, Phys. Rev. B 76 (15) (2007).
[15] K. Xu, Nonaqueous liquid electrolytes for lithium-based rechargeable batteries, Chem. Rev. 104 (2004) 4303–4417.
[16] R.S.M. Noel, Electrochemistry of graphite intercalation compounds, J. Power Sources 72 (1998) 53–65.
[17] M. Noel, V. Suryanarayanan, Role of carbon host lattices in Li-ion intercalation/De-intercalation processes, J. Power Sources 111 (2002) 193–209.
[18] D. Aurbach, B. Markovsky, I. Weissman, E. Levi, Y. Ein-Eli, On the correlation between surface chemistry and performance of graphite negative electrodes for Li Ion batteries, Electrochim. Acta 45 (1999) 671–686.
[19] D. Billaud, F.X. Henry, P. Willmann, Dependence of the morphology of graphitic electrodes on the electrochemical intercalation of lithium ions, J. Power Sources 54 (1995) 383–388.
[20] R. Yazami, Ph. Touzain, A reversible, graphite-lithium negative electrode for

electrochemical generators, J. Power Sources 9 (1983) 365–371.
[21] H. N., Kunihiro Nobuhara, Masafumi Nose, Shinji Nakanishi, Hideki Iba, First-principles study of alkali metal-graphite intercalation compounds, J. Power Sources 243 (2013) 585–587.
[22] Yoji Imai, Akio Watanabe, Energetic evaluation of possible stacking structures of Li-intercalation in graphite using a first-principle pseudopotential calculation, J. Alloys Compd. 439 (2007) 258–267.
[23] J. A, K. Rytkönen, M. Manninen, Density functional study of alkali-metal atoms and monolayers on graphite (0001), Phys. Rev. B 75 (2007) 075401.
[24] H. A., Shin'ichi Higai, Kunio Nishida, Nobuyuki Wada, Yukio Sakabe, Alkali-metal lithium on graphite monolayer surface: theoretical study, J. Phys. Chem. Solids 69 (2008) 1158–1161.
[25] Z.H. Zhu, G.Q. Lu, Comparative study of Li, Na, and K adsorptions on graphite by using ab initio method, Langmuir ACS J. Surfaces Colloids 20 (2004) 10751–10755.
[26] K.A. P., Eunseok Lee, Li absorption and intercalation in single layer graphene and few layer graphene by first principles, Nano Lett. 12 (2012) 4624–4628.
[27] F. Valencia, Lithium adsorption on graphite from density functional theory calculations, J. Phys. Chem. B 110 (2006) 14832–14841.
[28] W. W., C. Hartwigsen, E. Spohr, Charge density and charge transfer in stage-1 alkali-graphite intercalation compounds, Phys. Rev. B 55 (1997) 4953–4959.
[29] S. R., D.P. DiVincenzo, Theoretical investigation of the electronic properties of potassium graphite, Phys. Rev. B 25 (6) (1982) 4120–4125.
[30] Francesco Ancilotto, Flavio Toigo, First-principles study of potassium adsorption on graphite, Phys. Rev. B 47 (20) (1993) 13713–13721.
[31] M.M. I., Sascha Thinius, Paul Heitjans, Thomas Bredow, Theoretical study of Li migration in lithium–graphite intercalation compounds with dispersion-corrected DFT methods, J. Phys. Chem. C 118 (2014) 2273–2280.
[32] J. K., Ali Alavi, Michele Parrinello, Daan Frenkel, Ab initio molecular dynamics with excited electrons, Phys. Rev. Lett. 73 (1994) 2599.
[33] P.E. N., K.R. Kganyago, Effects of local and gradient-corrected density approximations on the prediction of the intralayer lattice distance *c*, in graphite and LiC_6, Mol. Simul. 22 (1999) 39–49.
[34] P.E. N., K.R. Kganyago, C.R.A. Catlow, Ab initio calculation of the voltage profile for LiC_6, Solid State Ion. 159 (2003) 21–23.
[35] M. Yamamoto, H. Imamura, First-principles calculation of graphite intercalation compound with density functional theory, Tanso 212 (2004) 81–90.
[36] L.J. S., W. Kohn, Self-consistent equations including exchange and correlation effects, Phys. Rev. 140 (1965) 1133.
[37] W. K., P. Hohenberg, Inhomogeneous electron gas, Phys. Rev. 136 (1964) 864.
[38] K. B., J.P. Perdew, M. Ernzerhof, Generalized gradient approximation made simple, Phys. Rev. Lett. 77 (1996) 3865.
[39] Stefan Grimme, Jens Antony, Stephan Ehrlich, Helge Krieg, Consistent and accurate ab initio parametrization of density functional dispersion correction (DFT-D) for the 94 elements H-Pu, J. Chem. Phys. 132 (2010) 154104.
[40] A. R., J.P. Perdew, G.I. Csonka, Restoring the density-gradient expansion for exchange in solids and surfaces, Phys. Rev. Lett. 100 (2008) 136406.
[41] R. C., Kari Laasonen, Changyol Lee, David Vanderbilt, Implementation of ultrasoft pseudo potentials in ab initio molecular dynamics, Phys. Rev. B 43 (1991) 6796.
[42] J.D. P., H.J. Monkhorst, Special points for Brillouin-zone integrations, Phys. Rev. B 13 (1976) 5188.
[43] Y. Li, B. Huang, X. Cheng, Y. Zhang, Achieving high specific capacity through a two-electron reaction in hypothetical Li_2VFSiO_4: a first-principles investigation, J. Electrochem. Soc. 162 (6) (2015) A787–A792.
[44] N. Govind, M. Petersen, G. Fitzgerald, D. King-Smith, J. Andzelm, A generalized synchronous transit method for transition state location, Comput. Mater. Sci. 28 (2) (2003) 250–258.
[45] G. Henkelman, B.P. Uberuaga, H. Jonsson, A climbing image nudged elastic band method for finding saddle points and minimum energy paths, J. Chem. Phys. 113 (22) (2000) 9901.
[46] P. Trucano, R. Chen, Structure of graphite by neutron diffraction, Nature 258 (1975) 136–137.
[47] D.E. Nixon, G.S. Parry, The expansion of the carbon-carbon bond length in potassium graphites, J. Phys. C 2 (1968) 1732.
[48] R.A. Jishi, M.S. Dresselhaus, Superconductivity in graphite intercalation compounds, Phys. Rev. B 45 (21) (1992) 12465–12469.
[49] D.E. N, G.S. Parry, The expansion of the carbon-carbon bond length in potassium graphites, J. Phys. C Solid State Phys. 2 (1969) 1732.
[50] M.S. Dresselhaus, G. Dresselhaus, Intercalation compounds of graphite, Adv. Phys. 30 (2) (1981) 139–326.
[51] L.W. Julio, C. Chacón-Torres, Thomas Pichler, Manifestation of charged and strained graphene layers in the raman response of graphite intercalation compounds, ACS Nano 7 (10) (2013) 9249–9259.
[52] Y. Okamoto, Density functional theory calculations of alkali metal (Li, Na, and K) graphite intercalation compounds, J. Phys. Chem. C 118 (1) (2014) 16–19.
[53] F.J. S, D. B, S. Aronson, Thermodynamic properties of the potassium–graphite lamellar compounds from solid-state emf measurements, J. Chem. Phys. 49 (1968) 434.
[54] A. Bianconi, S.B.M. Hagström, R.Z. Bachrach, Photoemission studies of graphite high-energy conduction-band and valence-band states using soft-X-ray synchrotron radiation excitation, Phys. Rev. B 16 (1977) 5531–5548.